ACS APPLIED MATERIALS & INTERFACES

www.acsami.org

Research Article

Symmetric Sodium-Ion Battery Based on Dual-Electron Reactions of NASICON-Structured $Na_3MnTi(PO_4)_3$ Material

Yu Zhou,○ Xiji Shao,○ Kwok-ho Lam, You Zheng, Lingzhi Zhao, Kedong Wang, Jinzhu Zhao,* Fuming Chen,* and Xianhua Hou*

Cite This: *ACS Appl. Mater. Interfaces* 2020, 12, 30328–30335

Read Online

ACCESS | Metrics & More | Article Recommendations | Supporting Information

ABSTRACT: Symmetric sodium-ion batteries possess promising features such as low cost, easy manufacturing process, and facile recycling post-process, which are suitable for the application of large-scale stationary energy storage. Herein, we proposed a symmetric sodium-ion battery based on dual-electron reactions of a NASICON-structured $Na_3MnTi(PO_4)_3$ material. The $Na_3MnTi(PO_4)_3$ electrode can deliver a stable capacity of up to 160 mAh g^{-1} with a Coulombic efficiency of 97% at 0.1 C by utilizing the redox reactions of $Ti^{3+/4+}$, $Mn^{2+/3+}$, and $Mn^{3+/4+}$. This is the first time to investigate the symmetric sodium-ion full cell using $Na_3MnTi(PO_4)_3$ as both cathode and anode in the organic electrolyte, demonstrating excellent reversibility and cycling performance with voltage plateaus of about 1.4 and 1.9 V. The full cell exhibits a reversible capacity of 75 mAh g^{-1} at 0.1 C and an energy density of 52 Wh kg^{-1}. In addition, both *ex situ* X-ray diffraction (XRD) analysis and first-principles calculations are employed to investigate the sodiation mechanism and structural evolution. The current research provides a feasible strategy for the symmetric sodium-ion batteries to achieve high energy density.

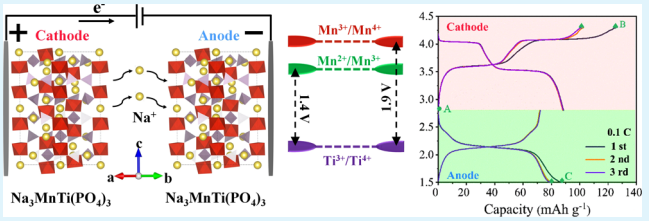

KEYWORDS: *sodium-ion batteries, symmetric full cell, $Na_3MnTi(PO_4)_3$, NASICON structure, multielectron redox reaction*

INTRODUCTION

With the consumption of oil and natural gas, the conversion of renewable energies like wind, solar, geothermal, etc. into usable energy forms is critical due to the clean and pollution-free characteristics.[1−4] In addition to energy conversion, storage is another challenge. Considerable efforts have been devoted to develop energy-storage devices, such as the lithium-ion batteries (LIBs).[5−8] Nowadays, LIBs are the most popular technology for energy storage, which are commercialized widely in various portable electronic devices, electric vehicles, etc.[9−14] However, LIBs have the drawback of high cost due to scarce availability of lithium resources. Therefore, sodium-ion batteries (SIBs) will be an emerging candidate to replace LIBs owing to the availability of sufficient raw material, safety, and low cost.[15−19] Recently, NASICON (Na superionic conductor)-structured materials are a hot research topic owing to the stable host structure, plenty of sodium-insertion interstices, and fast Na^+-ion diffusion. NASICON-structured polyanionic phosphates with a formula of $A_xMM'(PO_4)_3$ (A = Li, Na, K, etc.; M, M′ = transition-metal element) possess a robust three-dimensional framework of MO_6 and $M'O_6$ octahedral corner sharing with PO_4 tetrahedra, which delivers excellent cyclability.[20−25] Furthermore, the strong inductive effect of the phosphates endows multielectron redox reaction and higher operating potential versus Na^+/Na, compared to those of layered oxides.[26,27] $Na_3V_2(PO_4)_3$ is a typical NASICON-structured polyanionic phosphate that demonstrates two voltage plateaus at 1.6 and 3.3 V vs Na^+/Na, which correspond to the redox pairs of $V^{2+/3+}$ and $V^{3+/4+}$, resulting in dual-electron transfer.[28,29] So far, other kinds of phosphates have been synthesized via cation substitution partial or ful to develop redox reactions involving more than two electrons and excellent sodium-storage performance, including $Na_2VTi(PO_4)_3$, $Na_3V_{1.5}Cr_{0.5}(PO_4)_3$, $Na_3MnTi(PO_4)_3$, $Na_3FeV(PO_4)_3$, and $Na_2CrTi(PO_4)_3$.[26,30−33]

To date, the design of symmetric SIBs with the same electrode materials is progressively attractive compared to that of asymmetric batteries, owing to the less influence of matching design between cathode and anode materials, easy manufacturing process, facile recycling post-process, and low manufacturing cost.[34−37] In addition, symmetric SIBs based on the same intercalation-type compound are able to reduce the bulk expansion of electrode materials during Na^+ insertion/extraction because one electrode shrinks while the other electrode may expand, and vice versa.[38] At present, limited by the energy density, symmetric SIBs could be applied in storage power station, low-end electronic consumption, and low-speed

Received: March 28, 2020
Accepted: June 12, 2020
Published: June 12, 2020

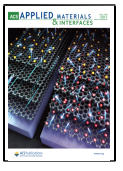

https://dx.doi.org/10.1021/acsami.0c05784
ACS Appl. Mater. Interfaces 2020, 12, 30328−30335

electric vehicles. NASICON-structured $Na_3MnTi(PO_4)_3$ has been reported recently, and its electrochemical performance is once studied in the aqueous system.[36] However, the operating voltage is limited owing to the potential window of water splitting with merely one Na^+ per formula extraction/insertion.[39] To date, symmetric sodium-ion battery in organic electrolyte with dual-electron transfer has not been reported yet.

In this work, the $Na_3MnTi(PO_4)_3$ electrode, prepared by a typical sol−gel method, delivers a reversible capacity of 160 mAh g^{-1} with a Coulombic efficiency of 97% under the voltage window of 1.5−4.3 V vs Na^+/Na at 0.1 C. This is the first time to investigate the dual-electron reactions of the symmetric sodium-ion full cell with $Na_3MnTi(PO_4)_3$ as both cathode and anode using the distinct of redox couples of $Ti^{3+/4+}$ and $Mn^{3+/4+}$. The symmetric full cell demonstrates excellent reversibility and cycling performance and exhibits a reversible capacity of 75 mAh g^{-1} at 0.1 C with energy densities of 52 Wh kg^{-1} and 60.4 mAh g^{-1} at 1 C. Moreover, theoretical investigation can be used to predict the voltage plateaus theoretically and estimate the configuration of the Na^+-site candidate under different occupation rates. Both *ex situ* X-ray diffraction (XRD) analysis and first-principles calculations are applied for studying the sodiation mechanism and structural evolution, indicating solid solution and two-phase reactions during Na^+ extraction/insertion. The proposed strategy is feasible for developing symmetric SIBs with high energy density.

EXPERIMENTAL SECTION

Preparation of $Na_3MnTi(PO_4)_3$. Carbon-coated $Na_3MnTi(PO_4)_3$ was prepared by the sol−gel method. $NaC_2H_3O_2$ (3 mmol), $MnC_4H_6O_4{\cdot}4H_2O$ (1 mmol), $NH_4H_2PO_4$ (3 mmol), and $C_6H_8O_7{\cdot}H_2O$ (3 mmol) were dissolved in 30 mL of deionized water to get Solution A. Titanium isopropoxide ($C_{12}H_{28}O_4Ti$, 1 mmol; Aladdin, 99.9% purity) was dissolved in 20 mL of absolute ethanol to obtain the transparent Solution B. Solution B was added into Solution A dropwise. The final solution was sealed and stirred in a water bath at 80 °C for 2 h and then uncovered until the moisture is completely evaporated to give a light-yellow precursor. The precursor was further kept in an oven and successively ground into powder. Finally, the precursor was sintered at 650 °C for 12 h under argon atmosphere at a heating rate of 5 °C·min^{-1} to obtain the $Na_3MnTi(PO_4)_3$ nanocomposite. The molar ratio of citric acid and transition metal (Ti and Mn) equaled 3:2, and citric acid was used as both chelating agent and carbon source.

Materials Characterization. The crystal structure of $Na_3MnTi(PO_4)_3$ was tested by X-ray diffraction (XRD) (Bruker D8 Advance with Cu/Kα radiation, λ = 0.15406 nm, 40 kV, 40 mA). Thermogravimetric (TG) analysis was employed to confirm the carbon content of materials. Raman measurements (RM) were performed on LabRAM HR Evolution with a laser wavelength of 532 nm. The morphology and distribution of elements were characterized by scanning electron microscopy (SEM, FEI Quanta 250 FEG). Energy-dispersive spectrometry (EDS) of a selected area was tested to analyze the chemical composition. Transmission electron microscopy (TEM) and selected area electron diffraction (SAED) images were obtained using a JEM-2100HR device. Cyclic voltammetry tests were carried out by a Solartron Analytical 1470E workstation. Electrochemical impedance spectroscopy (EIS) was performed under different charged/discharged states in the frequency of 1 mHz to 100 kHz.

Electrochemical Measurements. To study the electrochemical performances of the as-prepared $Na_3MnTi(PO_4)_3$, coin-type half-cells were assembled with sodium foil in a glovebox filled with argon (H_2O < 0.5 ppm, O_2 < 0.5 ppm). $Na_3MnTi(PO_4)_3$ active materials, super P conductive, and poly(vinylidene fluoride) binders with a weight ratio of 7:2:1 were dissolved in *N*-methylpyrrolidone (NMP) to obtain homogeneous slurries. The slurries were coated on aluminum foil and dried in a vacuum oven at 120 °C overnight to remove the solvent. The electrode film was then cut into a 12 mm diameter disk. The electrode loading mass was in the range of 1.2−1.5 mg cm^{-2}. Glass fiber (Whatman GF/C) was used as the separator. 1 M $NaClO_4$ dissolved in a solvent of ethylene carbonate (EC) and propylene carbonate (PC) (1:1 v/v) with 5 vol % addition of fluoroethylene carbonate (FEC) was used as the electrolyte. The electrochemical performance was tested on a Land battery analyzer within the cutoff voltage range of 1.5-4.3 V (vs Na/Na^+). Especially, without pretreatment processes, the symmetric battery with the same cathode and anode materials was directly assembled with the pristine $Na_3MnTi(PO_4)_3$ electrode. The battery was cathode-limited, and the capacity balance was controlled with the cathode/anode mass ratio of 1/1.25 (The charge specific capacity of the cathode was around 100 mA g^{-1}, and the discharge specific capacity of the anode was around 80 mA g^{-1}. Herein, the ratio of 100/80 was 1.25/1). The open-cell voltage of the symmetric full cell was approximately 0 V. 1 C corresponds to 117 mA g^{-1}.

RESULTS AND DISCUSSION

Theoretical Calculation of $Na_3MnTi(PO_4)_3$ Voltage Plateaus. The atomic structure of the supercell of $Na_xMnTi(PO_4)_3$ is shown in Figure 1a. PO_4 tetrahedron and MnO_6 (and TiO_6) octahedron share the oxygen atom at the corner. All of the possible sites are fully occupied for Na ions. To distinguish the sites of atoms, five groups are classified as colored in Figure 1b, depending on the symmetry and thermal stability of sodium ions. The calculation results are qualitatively displayed in Table S1.[40−43] Site-I is the most favorable location to occupy, and site-V is the least stable

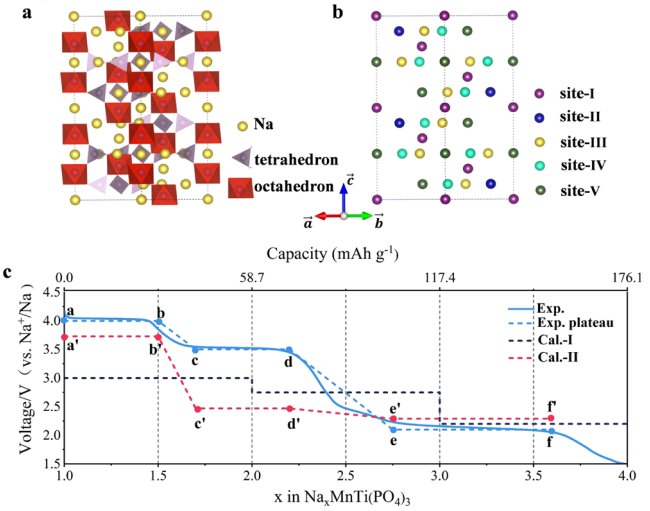

Figure 1. Theoretical calculation of voltage plateaus for $Na_3MnTi(PO_4)_3$. (a) Scheme plot of the atomic structure for the supercell of $Na_xMnTi(PO_4)_3$. Here, the fully occupied Na sites are shown (x = 5), while PO_4 tetrahedrons are highlighted with gray−purple, and MnO_6 (and TiO_6) octahedrons are highlighted with red color. (b) Five groups of Na sites are differed by colors, while the remaining sites are suppressed. (c) Calculated sodiation voltage profile (red and black dotted lines) in comparison to the experimental values (blue solid and dotted lines). The blue dotted line (exp. plateau) is simplified from the blue solid line (experimental curve). The black dotted line refers to the ideal case in which site-II, site-III, and site-IV are fully occupied one by one. The red dotted line is calculated using the experimental values of occupation rate for each plateau.

https://dx.doi.org/10.1021/acsami.0c05784
ACS Appl. Mater. Interfaces 2020, 12, 30328−30335

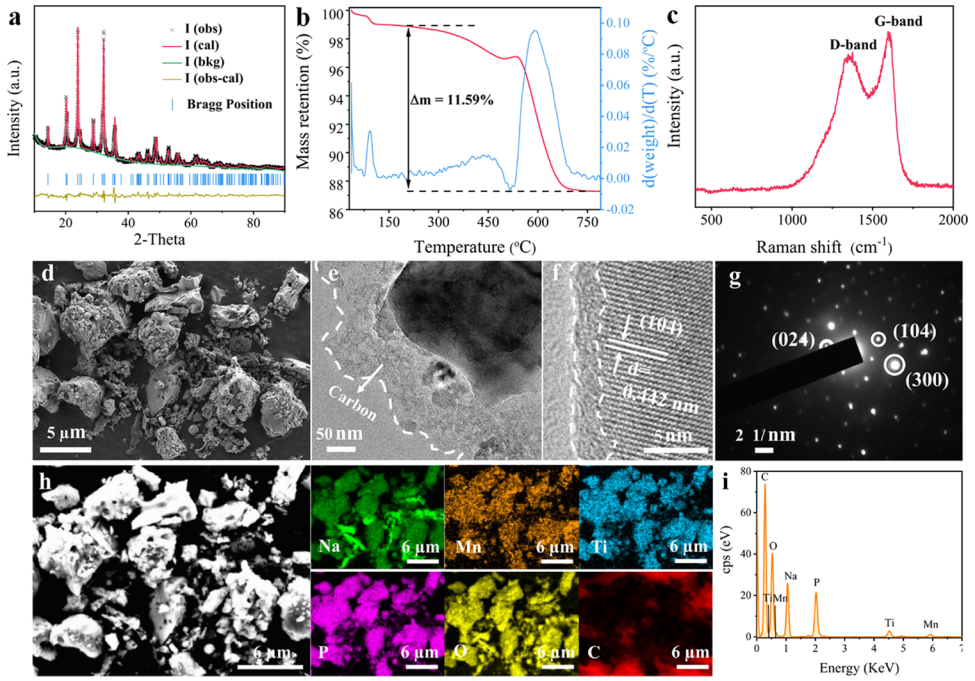

Figure 2. Crystal structure of $Na_3MnTi(PO_4)_3$ and characterization. (a) XRD pattern and Rietveld refinement, (b) TG curve, (c) Raman spectroscopy, (d) SEM image, (e) TEM image, (f) high-resolution (HR)TEM image, (g) SAED patterns, (h) elements mapping image, and (i) EDS image.

location. During the insertion/extraction process, Na ions at site-I will be immobilized to maintain the framework stability due to the most favorable energy, and Na ions at site-II, site-III, site-IV, and site-V are able to be inserted/extracted for electrochemical energy storage.[44] In our experiments, the occupation of site-V is not considered due to the least priority in the investigation.

During the discharging process from $Na_1MnTi(PO_4)_3$ to $Na_4MnTi(PO_4)_3$, three voltage plateaus are displayed at 4.0, 3.5, and 2.1 V vs Na^+/Na. Starting from the configuration $Na_1MnTi(PO_4)_3$ (x = 1), the occupation will follow the theoretical order, i.e., site-II, site-III, and then site-IV in sequence. Three ideal plateaus can be obtained as shown by the black dotted line (Cal.-I) in Figure 1c. When the current group is fully occupied, Na ions will go to the next group. However, there are still partial deviations on voltage plateaus, and their difference between the calculation and experimental results is shown by the blue solid line (Exp.). The main reasons can be given as follows: (1) The calculated group of sites is not fully occupied at voltage plateaus in practical experiments. When Na ions start to occupy a new site with different on-site energies, the voltage will shift to the next plateau like the plateau c,d for site-III and the plateau e,f for site-IV. (2) In the practical discharge process, the voltage moves from one plateau to another gradually, i.e., the ranges of b,c and d,e. It is contrary to the ideal calculated case in which the voltage jumps from one plateau to another discontinuously. In the intermediate region, Na ions would occupy sites with different on-site energies, while the experimental values are the dynamic average of them.

To further analyze the voltage evolution, the experimental value of x for each plateau is selected for re-simulation. The updated result, see the red dotted line (Cal.-II), fits better the trend of experimental results. It is worth to point out that the calculated voltage value strongly depends on the value of x and the corresponding configurations. At this stage, it is relatively easy to estimate the configurations at two ends such as Points a, b, e, and f. Nevertheless, the calculated voltage of the c′,d′ plateau is still far less than the experimental one, which requires a substantial detailed study to give the accurate atomic structures of Points c and d. Theoretical studies do not only predict the voltage plateaus but also provide valuable clues to qualitatively understand the mechanism of charge/discharge process in $Na_xMnTi(PO_4)_3$.

Crystal Structure of $Na_3MnTi(PO_4)_3$ and Characterizations. The crystal structure analysis and characterization of $Na_3MnTi(PO_4)_3$ are demonstrated in Figure 2. Rietveld refinement of the X-ray diffraction (XRD) pattern shows the successful preparation of $Na_3MnTi(PO_4)_3$ by a facile sol–gel method in Figure 2a. The pattern can be indexed to the rhombohedral structure with lattice parameters of a = 8.73352 Å and c = 21.84703 Å and a reliable result of R = 4.32%, exhibiting little discrepancy to that of $Na_3V_2(PO_4)_3$.[45] $Na_3MnTi(PO_4)_3$ possesses a typical rhombohedral NASICON-type structure with space group $R\bar{3}c$.[46] The detailed structural information including lattice parameters and site occupancy factor is presented in Table S2 (Supporting Information). The carbon amount of 11.59% is confirmed by the thermogravimetric (TG) analysis (Figure 2b). A slight increase in weight around 500 °C is attributed to the oxidation of low-valence-state metal species during the combustion of carbon. Raman spectroscopy (Figure 2c) is utilized to qualitatively study the degree of graphitization in $Na_3MnTi(PO_4)_3$. The G-band and D-band of carbon materials are located at 1594.7 and 1348.3 cm^{-1}, respectively. The ratio of I_G/I_D = 1.14 (the intensity ratio of 2394/2090) indicates the existence of amorphous carbon in pristine $Na_3MnTi(PO_4)_3$.[26,46]

The morphology of $Na_3MnTi(PO_4)_3$ is obtained by SEM, as shown in Figure 2d. $Na_3MnTi(PO_4)_3$ has a wide range of

https://dx.doi.org/10.1021/acsami.0c05784
ACS Appl. Mater. Interfaces 2020, 12, 30328–30335

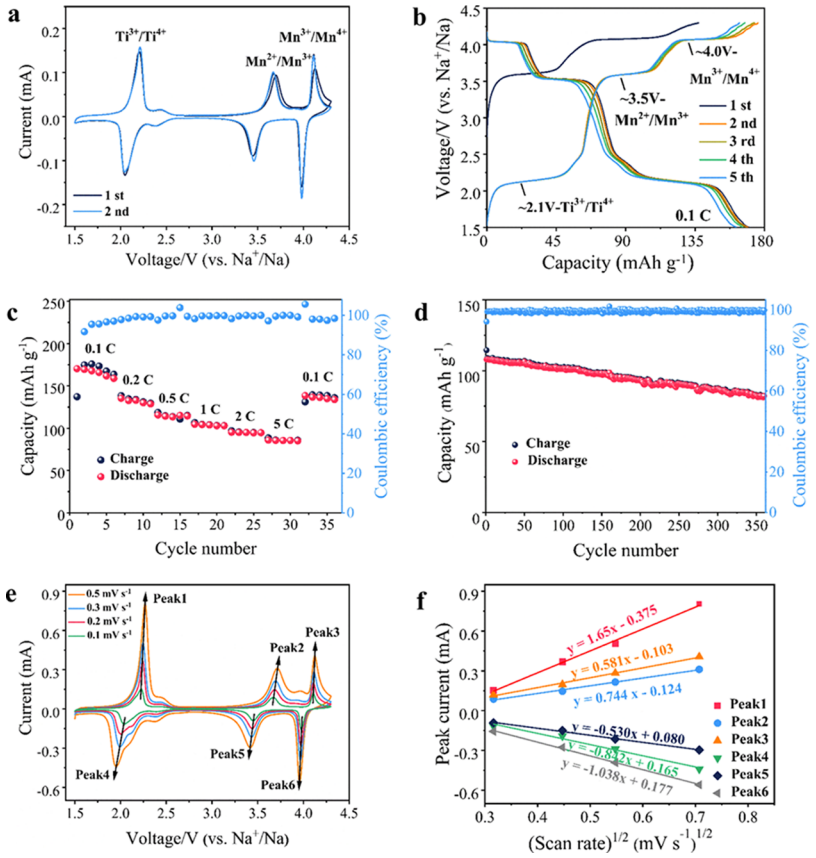

Figure 3. Sodium-ion storage performance and kinetic properties of $Na_3MnTi(PO_4)_3$ with Na counter. (a) Cyclic voltammogram curves between 1.5 and 4.3 V at a scan rate of 0.1 mV s^{-1}. (b) Galvanostatic charge−discharge profiles in the initial five cycles between 1.5 and 4.3 V at 0.1 C (1 C = 117 mA g^{-1}). (c) Rate capability from 0.1 to 5 C. (d) Cycling performance at 5 C. (e) Cyclic voltammogram curves at different scanning rates. (f) Relationship between the peak current (I_p) and the square root of the scan rate ($v^{1/2}$).

particle size from few nanometers to micrometer. The matching of different particle sizes is beneficial to the physical contact between particles, resulting in high density. TEM analysis is conducted to further confirm the composition of the amorphous carbon and $Na_3MnTi(PO_4)_3$. As shown in Figure 2e, $Na_3MnTi(PO_4)_3$ particles are embedded in an amorphous carbon matrix. The high-resolution HRTEM (Figure 2f) image manifests that the surface of well-crystallized $Na_3MnTi(PO_4)_3$ is coated by a thin layer of uniform amorphous carbon with ∼3 nm thickness from the pyrolysis of critic acid. The observed lattice fringe of 0.442 nm is consistent with the interplanar spacing plane (104). Selected area electron diffraction (SAED) in Figure 2g is employed to further explore the structure of $Na_3MnTi(PO_4)_3$, which exhibits (024), (104), and (300) planes for the rhombohedral structure. These agree with the XRD results. Element mapping in Figure 2h and energy-dispersive spectra (EDS) in Figure 2i of selected area are tested to analyze the chemical composition. The distribution of homogeneous elements of Na, Mn, Ti, P, and O can be observed as displayed. Based on the EDS results, no other elements are detected and the atomic ratio of Na:Mn:Ti is equal to 3.5:1.06:1. The amorphous carbon layer on the surface of $Na_3MnTi(PO_4)_3$ particles will promote the electron transfer owing to the low electrical conductivity of NASICON-structured phosphates.[23,31,47]

Sodium-Ion Storage Performance and Kinetic Properties of $Na_3MnTi(PO_4)_3$. The electrochemical performance of the as-prepared $Na_3MnTi(PO_4)_3$ is evaluated by assembling the CR2032-type half-cell with sodium counter. Cyclic voltammogram (CV) tests are carried out to investigate the redox activities of $Na_3MnTi(PO_4)_3$. As shown in Figure 3a, the initial three CV cycles are recorded with a scan rate of 0.1 mV s^{-1} between 4.3 and 1.5 V. Three pairs of redox couples are located at around 2.04/2.22, 3.46/3.66, and 3.99/4.10 V, respectively, which also correspond to a three-step transition of the Na^+ extraction/insertion due to the redox reactions of $Ti^{3+/4+}$, $Mn^{2+/3+}$, and $Mn^{3+/4+}$. The electrochemical impedance spectra (EIS) are tested to understand the difference in different voltage conditions. As represented in Figure S1 and Table S3 (Supporting Information), according to the equivalent circuit, the charge-transfer resistances (R_{ct}) do not change a lot at different charged/discharged states, which can be attributed to the physical properties of carbon-coated NASICON structure, particularly the better conductivity. The evolution processes are further analyzed in detail using *ex situ* XRD with different charge/discharge states between 4.3 and 1.5 V, as shown in Figure S2 (Supporting Information). The whole Na^+ extraction or insertion process refers to two-phase evolution and solid solution reactions (single-phase evolution).[46,48] As depicted in Figure 3b, in the first charge process, two plateaus are displayed, corresponding to dual-electron reactions. This low capacity may be attributed to the high initial open-circuit voltage of up to 2.6−2.8 V. Afterward, in the following charge cycles, three charge voltage plateaus are located at 2.1, 3.5, and 4.0 V vs Na^+/Na, which are consistent with three oxidation couples of Ti^{3+} to Ti^{4+}, Mn^{2+} to Mn^{3+}, and

https://dx.doi.org/10.1021/acsami.0c05784
ACS Appl. Mater. Interfaces 2020, 12, 30328−30335

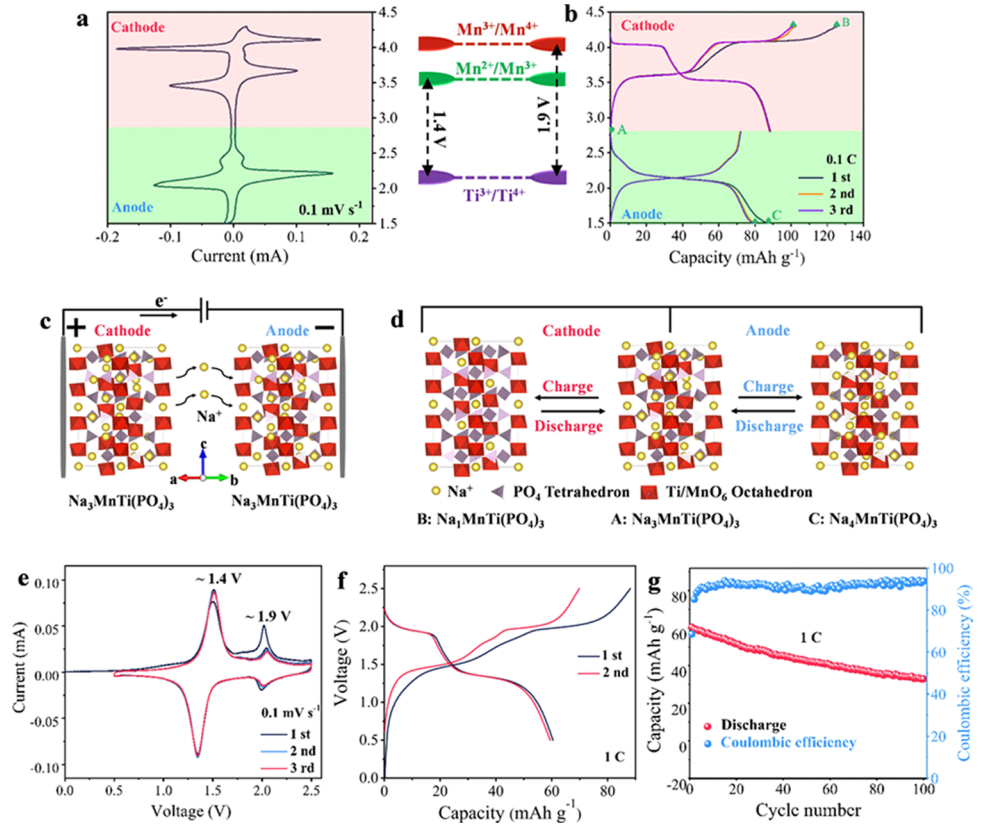

Figure 4. (a) Half-cell charge/discharge voltage curves and (b) voltage capacity profiles within different potential regions (A: pristine $Na_3MnTi(PO_4)_3$; B: charge to 4.3 V, $Na_1MnTi(PO_4)_3$; C: discharge to 1.5 V, $Na_4MnTi(PO_4)_3$). (c) Schematic illustration of $Na_3MnTi(PO_4)_3$||$Na_3MnTi(PO_4)_3$ symmetric SIBs. (d) Schematic diagram of unit cells of cathode and anode during the charge/discharge process. (e) Cyclic voltammogram curves of symmetric sodium-ion battery, (f) charge/discharge curves, and (g) cycling performance at 1 C for the symmetric batteries.

Mn^{3+} to Mn^{4+}, respectively. $Na_3MnTi(PO_4)_3$ delivers an initial charge specific capacity of 137.2 mAh g^{-1}, and the initial discharge specific capacity is 170.3 mAh g^{-1}. In the subsequent cycles, a stable discharge specific capacity of 160 mAh g^{-1} can be obtained with a Coulombic efficiency (CE) of 97%, indicating the superior reversible stability. The results are in good agreement with the voltage plateaus in Figure 3a. The rate capability in Figure 3c demonstrates the reversible capacities of 169.4, 135.4, 115.7, 104.7, 95.3, and 86.0 mAh g^{-1} at 0.1, 0.2, 0.5, 1, 2, and 5 C, respectively. The corresponding charge and discharge profiles are shown in Figure S3 (Supporting Information), and all curves exhibit three voltage plateaus. Both the highest-voltage plateau and capacity decay with the rate increase, possibly resulting from the polarization. When the rate returns to 0.1 C, the discharge capacity of 138.5 mAh g^{-1} is obtained with capacity retentions of 82% and ~100% CE, indicating the excellent rate capability. Long-term stability is demonstrated in Figure 3d. The discharge capacity of 107.9 mAh g^{-1} is delivered at 5 C with a capacity retention of 76.2% after 360 cycles. Figure S4 (Supporting Information) displays the corresponding charge and discharge profiles at different cycles.

To get an insight into the kinetic behaviors, CV tests with different scanning rates from 0.1 to 0.5 mV s^{-1} are conducted, as shown in Figure 3e. The peak current increases with the increasing scan rate, in which the linear relationship between the peak currents (I_p) and the square root of the scanning rate ($v^{1/2}$) is plotted to estimate the diffusion coefficient (D_{Na^+}) in Figure 3f using the following equation[49]

$$I_p = 2.69 \times 10^5 n^{3/2} A D_{Na^+}^{1/2} C_{Na} v^{1/2} \quad (1)$$

where I_p, n, A, C_{Na}, and v are the peak current, number of exchanged electrons per formula during the reactions, effective reaction area (1.13 cm^2), Na^+ concentration in the electrode, and scan rate, respectively. During the anodic scan, D_{Na^+} values for peak 1, peak 2, and peak 3 are 3.86×10^{-11}, 3.14×10^{-11}, and 7.66×10^{-11} cm^2 s^{-1}, respectively. During the cathodic scan, D_{Na^+} values for peak 4, peak 5, and peak 6 are 1.00×10^{-11}, 1.59×10^{-11}, and 2.44×10^{-10} cm^2 s^{-1}, respectively. Peak 3 and peak 6 show the largest D_{Na^+} values in anodic and cathodic scans, indicating that the structural evolution of $Na_2MnTi(PO_4)_3 \leftrightarrow Na_1MnTi(PO_4)_3$ is the most favorable with the fastest ion diffusion compared to other two evolution processes. The results agree well with the Na^+ insertion/extraction energy results in density functional theory (DFT) calculation, which indicates that the site-I and site-II are the most favorable sites for sodium ions to diffuse, relating to the configurations $Na_1MnTi(PO_4)_3$ and $Na_2MnTi(PO_4)_3$ (Table S1, Supporting Information).

Sodium-ion storage can be defined as two processes: diffusion reactions of faradic contribution and redox process of pseudocapacitance. The effect of the pseudocapacitance for the battery reaction system can be explored by the following equations[30,50]

https://dx.doi.org/10.1021/acsami.0c05784
ACS Appl. Mater. Interfaces 2020, 12, 30328−30335

$$I_p = av^b \quad (2)$$

$$\log I_p = \log a + b \log v \quad (3)$$

where a and b are adjustable parameters, I_p is the peak current, and v is the scan rate. For a pesudocapacitance-controlled process, the b-value is close to or above 1, while for the electrochemical diffusion-dominated process, the b-value is around 0.5. In Figure S5 (Supporting Information), all b-values are above 0.5, indicating the coexistent behaviors of diffusion and pesudocapacitance within the $Na_3MnTi(PO_4)_3$ electrode. It should be noted that the pseudocapacitance reaction is conducive to the rate capability and cycling performance.

Electrochemical Performance of the Symmetric Sodium-Ion Battery in Organic Electrolyte. The charge/discharge voltage plots and voltage matchup of $Na_3MnTi(PO_4)_3$ half-cell within different voltage regions are shown in Figure 4a,b. The $Ti^{3+/4+}$ redox pair at 2.1 V and $Mn^{2+/3+}$ and $Mn^{3+/4+}$ pairs at 3.5 and 4.0 V indicate that $Na_3MnTi(PO_4)_3$ is able to serve as both anode and cathode materials. For the cathode part, it exhibits the extraction/insertion of two Na^+ (A ↔ B = $Na_3MnTi(PO_4)_3$ ↔ $Na_1MnTi(PO_4)_3$) and delivers an initial charge capacity of 125.6 mAh g^{-1} with a stable charge capacity of about 100 mAh g^{-1}. As for the anode part, it relates to the reversible one Na^+ insertion into $Na_3MnTi(PO_4)_3$, leading to the phase of $Na_4MnTi(PO_4)_3$ (C) at 2.1 V with an initial discharge capacity of 87.4 mAh g^{-1} and a stable discharge capacity of about 80 mAh g^{-1}.

Benefiting from the potential difference between $Mn^{3+/4+}$, $Mn^{2+/3+}$, and $Ti^{3+/4+}$ redox pairs, a symmetric battery based on the dual-electron reactions is constructed with $Na_3MnTi(PO_4)_3$||$NaClO_4$ (1 M)||$Na_3MnTi(PO_4)_3$. The schematic illustration of symmetric SIBs is demonstrated in Figure 4a. There is no pretreatment for both cathode and anode electrodes during the fabrication of symmetric battery. Figure 4b illustrates the respective reactions and evolution of cathode (A ↔ B) and anode (A ↔ C) during the charge/discharge process. Herein, the reactions of cathode and anode during the charging ↔ discharging process can be identified as follows

$$\text{Cathode: } Na_3MnTi(PO_4)_3 \leftrightarrow Na_1MnTi(PO_4)_3 + 2Na^+ + 2e^- \quad (4)$$

$$\text{Anode: } Na_3MnTi(PO_4)_3 + Na^+ + e^- \leftrightarrow Na_4MnTi(PO_4)_3 \quad (5)$$

Cyclic voltammogram curves (Figure 4e) exhibit two pairs of obvious redox peaks at ∼1.4 and ∼1.9 V, confirming the dual-electron redox reactions for the $Na_3MnTi(PO_4)_3$ symmetric battery, which are consistent with the voltage gaps in Figure 4a,b. The low-voltage plateau is derived from the voltage gap of 2.1 V ($Ti^{3+/4+}$) and 3.5 V ($Mn^{2+/3+}$), and the high voltage plateau of ∼1.9 V is dominantly originated from the contribution of 2.1 V ($Ti^{3+/4+}$) and $Mn^{3+/4+}$ (4.0 V), which is relatively high compared to the reported values in various types of symmetric batteries with the NASCION-structured material (Table S4, Supporting Information). The first two charge−discharge profiles and the corresponding cycling performance at 1 C are illustrated in Figures 4f,g and S6 (Supporting Information), which deliver an initial discharge capacity of 60.4 mAh g^{-1} and a capacity retention of 54.5% after 100 cycles. The cycling stability at 1 C is not very high, which is mainly attributed to the polarization and slightly low Columbic efficiency. The capacity−voltage profiles of the $Na_3MnTi(PO_4)_3$ symmetric battery at 0.1 C are shown in Figure S7 (Supporting Information). The initial charge and discharge capacities are 116.3 and 72.9 mAh g^{-1}, respectively. The energy density is 52 Wh kg^{-1}. Except the first cycle, the subsequent neighbor cycles can be overlapped well, indicating the excellent reversibility. Figure S8 (Supporting Information) demonstrates the charge/discharge curves at different rates. The discharge capacities of 76.1, 67.0, 58.9, 51.7, 44.4, and 34.5 mAh g^{-1} can be obtained of 0.1, 0.2, 0.5, 1, 2, and 5 C, respectively. The promising performance is mainly attributed to the symmetric nature, abating the volume expansion of electrodes during the sodiation/desodiation process. Besides, the characters of fast electron and ionic conductivity of carbon-coated NASICON-structured materials strongly generate a positive impact on sodium-storage performance. Furthermore, based on the transition-metal multivalence status, NASICON-structured symmetric batteries with a higher energy density could be achieved by matching higher and lower transition-metal redox couples.

CONCLUSIONS

A NASICON-structured $Na_3MnTi(PO_4)_3$ is prepared through a facile sol−gel method and displays a stable capacity of 160 mAh g^{-1} with a Coulombic efficiency of 97% at 0.1 C. The three voltage plateaus of 2.1, 3.5, and 4.0 V vs Na^+/Na correspond to the redox pairs of $Ti^{3+/4+}$, $Mn^{2+/3+}$, and $Mn^{3+/4+}$, respectively. By utilizing the voltage difference between three redox pairs, the current symmetric sodium-ion full cell with $Na_3MnTi(PO_4)_3$ as both cathode and anode achieves dual-electron reactions and a high operating voltage, leading to a high energy density. It exhibits a stable discharge capacity of about 75 mAh g^{-1} at 0.1 C and 60.4 mAh g^{-1} at 1 C, indicating the good reversibility and cycling performance. The operating voltage of 1.9 V and an improved energy density of 52 Wh kg^{-1} are obtained. Moreover, the agreement between experimental and DFT investigations does not only provide better understanding of the sodiation mechanism but also show the potential pathway of designing the voltage plateaus by tuning the occupation of carriers. Our research highlights the prospect of NASICON-structured symmetric batteries based on multi-electron reactions to improve sodium-storage performance for high energy density.

ASSOCIATED CONTENT

Supporting Information

The Supporting Information is available free of charge at https://pubs.acs.org/doi/10.1021/acsami.0c05784.

DFT details; detailed crystal structure; EIS results; and capacity−voltage profiles of $Na_3MnTi(PO_4)_3$ half-cell and symmetric full cell (PDF)

AUTHOR INFORMATION

Corresponding Authors

Jinzhu Zhao − *Guangdong Provincial Key Laboratory of Quantum Engineering and Quantum Materials, Guangdong Engineering Technology Research Center of Efficient Green Energy and Environment Protection Materials, School of Physics and Telecommunication Engineering, South China Normal University, Guangzhou 510006, P. R. China; Center for Computational Science and Engineering, Southern University of Science and Technology, Shenzhen 518055, China;*

https://dx.doi.org/10.1021/acsami.0c05784
ACS Appl. Mater. Interfaces 2020, 12, 30328−30335

orcid.org/0000-0003-1841-1302;
Phone: +862039318011; Email: zhaojz@m.scnu.edu.cn

Fuming Chen − *Guangdong Provincial Key Laboratory of Quantum Engineering and Quantum Materials, Guangdong Engineering Technology Research Center of Efficient Green Energy and Environment Protection Materials, School of Physics and Telecommunication Engineering and National and Local Joint Engineering Research Center of Key Materials and Technologies for High Energy and Safety Batteries. Engineering Research Center of MTEES (Ministry of Education), South China Normal University, Guangzhou 510006, P. R. China;* orcid.org/0000-0002-0108-9831; Email: fmchen@m.scnu.edu.cn

Xianhua Hou − *Guangdong Provincial Key Laboratory of Quantum Engineering and Quantum Materials, Guangdong Engineering Technology Research Center of Efficient Green Energy and Environment Protection Materials, School of Physics and Telecommunication Engineering and National and Local Joint Engineering Research Center of Key Materials and Technologies for High Energy and Safety Batteries. Engineering Research Center of MTEES (Ministry of Education), South China Normal University, Guangzhou 510006, P. R. China;* orcid.org/0000-0003-4305-5143; Email: houxianhua@m.scnu.edu.cn

Authors

Yu Zhou − *Guangdong Provincial Key Laboratory of Quantum Engineering and Quantum Materials, Guangdong Engineering Technology Research Center of Efficient Green Energy and Environment Protection Materials, School of Physics and Telecommunication Engineering and National and Local Joint Engineering Research Center of Key Materials and Technologies for High Energy and Safety Batteries. Engineering Research Center of MTEES (Ministry of Education), South China Normal University, Guangzhou 510006, P. R. China*

Xiji Shao − *Department of Physics, Southern University of Science and Technology, Shenzhen 518055, China; Harbin Institute of Technology, Harbin 150080, China*

Kwok-ho Lam − *Department of Electrical Engineering, The Hong Kong Polytechnic University, Hung Hom, Kowloon, Hong Kong*

You Zheng − *Guangdong Provincial Key Laboratory of Quantum Engineering and Quantum Materials, Guangdong Engineering Technology Research Center of Efficient Green Energy and Environment Protection Materials, School of Physics and Telecommunication Engineering, South China Normal University, Guangzhou 510006, P. R. China*

Lingzhi Zhao − *SCNU Qingyuan Institute of Science and Technology Innovation Co., Ltd., Qingyuan 511517, China*

Kedong Wang − *National and Local Joint Engineering Research Center of Key Materials and Technologies for High Energy and Safety Batteries. Engineering Research Center of MTEES (Ministry of Education), South China Normal University, Guangzhou 510006, P. R. China;* orcid.org/0000-0003-1253-5603

Complete contact information is available at: https://pubs.acs.org/10.1021/acsami.0c05784

Author Contributions

○Y.Z. and X.S. contributed equally to this work.

Notes

The authors declare no competing financial interest.

■ ACKNOWLEDGMENTS

This work was financially supported by the union project of National Natural Science Foundation of China and Guangdong Province (U1601214), National Natural Science Foundation of China (NSFC, grant nos. 11404159 and 11704177), the Science and Technology Planning Project of Guangdong Province (2018B050502010, 2018A050506078, 2017B090901027, 2019B090905005), the Challenge Cup Gold Seed cultivation Project of South China Normal University (19WDKB01) and the Pearl River Talent Program (2019QN01L951).

■ REFERENCES

(1) Chen, F.; Huang, Y.; Guo, L.; Sun, L.; Wang, Y.; Yang, H. Y. Dual-ions Electrochemical Deionization: a Desalination Generator. *Energy Environ. Sci.* **2017**, *10*, 2081−2089.

(2) Zhang, W.; Li, Y.; Zhou, L.; Zheng, Q.; Xie, F.; Lam, K. H.; Lin, D. Ultrathin Amorphous CoFeP Nanosheets Derived from CoFe LDHs by Partial Phosphating as Excellent Bifunctional Catalysts for Overall Water Splitting. *Electrochim. Acta* **2019**, *323*, No. 134595.

(3) Fan, L.; Ma, R.; Zhang, Q.; Jia, X.; Lu, B. Graphite Anode for a Potassium-Ion Battery with Unprecedented Performance. *Angew. Chem., Int. Ed.* **2019**, *58*, 10500−10505.

(4) Liu, J. Addressing the Grand Challenges in Energy Storage. *Adv. Funct. Mater.* **2013**, *23*, 924−928.

(5) Hu, Q.; Jiang, X.; He, M.; Zheng, Q.; Lam, K. H.; Lin, D. Core-shell Nanostructured MnO_2@Co_9S_8 Arrays for High-performance Supercapacitors. *Electrochim. Acta* **2020**, *338*, No. 135896.

(6) Fan, L.; Chen, S.; Zhu, J.; Ma, R.; Li, S.; Podila, R.; Rao, A. M.; Yang, G.; Wang, C.; Liu, Q.; Xu, Z.; Yuan, L.; Huang, Y.; Lu, B. Simultaneous Suppression of the Dendrite Formation and Shuttle Effect in a Lithium-Sulfur Battery by Bilateral Solid Electrolyte Interface. *Adv. Sci.* **2018**, *5*, No. 1700934.

(7) Zhang, Z.; Hu, X.; Zhou, Y.; Wang, S.; Yao, L.; Pan, H.; Su, C.-Y.; Chen, F.; Hou, X. Aqueous Rechargeable Dual-ion Battery Based on Fluoride Ion and Sodium Ion Electrochemistry. *J. Mater. Chem. A* **2018**, *6*, 8244−8250.

(8) Li, S.; Dong, Y.; Xu, L.; Xu, X.; He, L.; Mai, L. Effect of Carbon Matrix Dimensions on the Electrochemical Properties of $Na_3V_2(PO_4)_3$ Nanograins for High-Performance Symmetric Sodium-Ion Batteries. *Adv. Mater.* **2014**, *26*, 3545−3553.

(9) He, Z.; Jiang, Y.; Zhu, J.; Li, Y.; Jiang, Z.; Zhou, H.; Meng, W.; Wang, L.; Dai, L. Boosting the Performance of $LiTi_2(PO_4)_3$/C Anode for Aqueous Lithium Ion Battery by Sn Doping on Ti Sites. *J. Alloys Compd.* **2018**, *731*, 32−38.

(10) Zhou, Y.; Hou, X.; Shen, K.; Wang, S.; Chen, F.; Li, Y.; Chen, H.; Wang, B. $Li_{1.1}Na_{0.1}Mn_{0.534}Ni_{0.133}Co_{0.133}O_2$ as Cathode with Ameliorated Electrochemical Performance Based on Dual Li^+/Na^+ Electrolyte. *Ionics* **2019**, *25*, 51−59.

(11) Shi, L.; Zeng, F.; Cheng, X.; Lam, K. H.; Wang, W.; Wang, A.; Jin, Z.; Wu, F.; Yang, Y. Enhanced Performance of Lithium-Sulfur Batteries with High Sulfur Loading Utilizing Ion Selective MWCNT/SPANI Modified Separator. *Chem. Eng. J.* **2018**, *334*, 305−312.

(12) Luo, J. Y.; Xia, Y. Y. Aqueous Lithium-ion Battery $LiTi_2(PO_4)_3$/$LiMn_2O_4$ with High Power and Energy Densities as well as Superior Cycling Stability. *Adv. Funct. Mater.* **2007**, *17*, 3877−3884.

(13) Li, Y.; Hou, X.; Zhou, Y.; Han, W.; Liang, C.; Wu, X.; Wang, S.; Ru, Q. Electrochemical Performance of Structure-Dependent $LiNi_{1/3}Co_{1/3}Mn_{1/3}O_2$ in Aqueous Rechargeable Lithium-Ion Batteries. *Energy Technol.* **2018**, *6*, 391−396.

(14) Hu, Y.; Ding, H.; Bai, Y.; Liu, Z.; Chen, S.; Wu, Y.; Yu, X.; Fan, L.; Lu, B. Rational Design of a Polyimide Cathode for a Stable and High-Rate Potassium-Ion Battery. *ACS Appl. Mater. Interfaces* **2019**, *11*, 42078−42085.

(15) Senguttuvan, P.; Rousse, G.; Arroyo y de Dompablo, M. E.; Vezin, H.; Tarascon, J. M.; Palacin, M. R. Low-Potential Sodium

Insertion in a NASICON-Type Structure through the Ti(III)/Ti(II) Redox Couple. *J. Am. Chem. Soc.* **2013**, *135*, 3897−3903.
(16) Liu, T.; Zhang, Y.; Chen, C.; Lin, Z.; Zhang, S.; Lu, J. Sustainability-Inspired Cell Design for a Fully Recyclable Sodium Ion Battery. *Nat. Commun.* **2019**, *10*, No. 1965.
(17) Wang, X.; Wang, S.; Shen, K.; He, S.; Hou, X.; Chen, F. Phosphorus-Doped Porous Hollow Carbon Nanorods for High-Performance Sodium-Based Dual-Ion batteries. *J. Mater. Chem. A* **2020**, *8*, 4007−4016.
(18) Li, H.; Jin, T.; Chen, X.; Lai, Y.; Zhang, Z.; Bao, W.; Jiao, L. Rational Architecture Design Enables Superior Na Storage in Greener NASICON-$Na_4MnV(PO_4)_3$ Cathode. *Adv. Energy Mater.* **2018**, *8*, No. 1801418.
(19) Niu, Y. B.; Yin, Y. X.; Guo, Y. G. Nonaqueous Sodium-Ion Full Cells: Status, Strategies, and Prospects. *Small* **2019**, *15*, No. e1900233.
(20) Zhao, L.; Zhao, H.; Du, Z.; Wang, J.; Long, X.; Li, Z.; Świerczek, K. Delicate Lattice Modulation Enables Superior Na Storage Performance of $Na_3V_2(PO_4)_3$ as both an Anode and Cathode Material for Sodium-Ion Batteries: Understanding the Role of Calcium Substitution for Vanadium. *J. Mater. Chem. A* **2019**, *7*, 9807−9814.
(21) Zhao, W.; Guo, L.; Ding, M.; Huang, Y.; Yang, H. Y. Ultrahigh-Desalination-Capacity Dual-Ion Electrochemical Deionization Device Based on $Na_3V_2(PO_4)_3$@C-AgCl Electrodes. *ACS Appl. Mater. Interfaces* **2018**, *10*, 40540−40548.
(22) Kawai, K.; Asakura, D.; Nishimura, S. I.; Yamada, A. Stabilization of a 4.5 V $Cr^{(4+)}/Cr^{(3+)}$ Redox Reaction in NASICON-Type $Na_3Cr_2(PO_4)_3$ by Ti Substitution. *Chem. Commun.* **2019**, *55*, 13717−13720.
(23) Ramesh Kumar, P.; Kheireddine, A.; Nisar, U.; Shakoor, R. A.; Essehli, R.; Amin, R.; Belharouak, I. $Na_4MnV(PO_4)_3$-rGO as Advanced Cathode for Aqueous and Non-Aqueous Sodium Ion Batteries. *J. Power Sources* **2019**, *429*, 149−155.
(24) Kawai, K.; Zhao, W.; Nishimura, S.-i.; Yamada, A. High-Voltage Cr^{4+}/Cr^{3+} Redox Couple in Polyanion Compounds. *ACS Appl. Energy Mater.* **2018**, *1*, 928−931.
(25) Zhang, L.; Zhang, B.; Wang, C.; Dou, Y.; Zhang, Q.; Liu, Y.; Gao, H.; Al-Mamun, M.; Pang, W. K.; Guo, Z.; Dou, S. X.; Liu, H. K. Constructing the Best Symmetric Full K-ion Battery with the NASICON-Type $K_3V_2(PO_4)_3$. *Nano Energy* **2019**, *60*, 432−439.
(26) Wang, D.; Bie, X.; Fu, Q.; Dixon, D.; Bramnik, N.; Hu, Y. S.; Fauth, F.; Wei, Y.; Ehrenberg, H.; Chen, G.; Du, F. Sodium Vanadium Titanium Phosphate Electrode for Symmetric Sodium-Ion Batteries with High Power and Long Lifespan. *Nat. Commun.* **2017**, *8*, No. 15888.
(27) Wang, P.-F.; You, Y.; Yin, Y.-X.; Guo, Y.-G. Layered Oxide Cathodes for Sodium-Ion Batteries: Phase Transition, Air Stability, and Performance. *Adv. Energy Mater.* **2018**, No. 1701912.
(28) Yao, X.; Zhu, Z.; Li, Q.; Wang, X.; Xu, X.; Meng, J.; Ren, W.; Zhang, X.; Huang, Y.; Mai, L. 3.0 V High Energy Density Symmetric Sodium-Ion Battery: $Na_4V_2(PO_4)_3$ parallel $Na_3V_2(PO_4)_3$. *ACS Appl. Mater. Interfaces* **2018**, *10*, 10022−10028.
(29) Guo, J. Z.; Wang, P. F.; Wu, X. L.; Zhang, X. H.; Yan, Q.; Chen, H.; Zhang, J. P.; Guo, Y. G. High-Energy/Power and Low-Temperature Cathode for Sodium-Ion Batteries: In Situ XRD Study and Superior Full-Cell Performance. *Adv. Mater.* **2017**, *29*, No. 1701968.
(30) Zhao, Y.; Gao, X.; Gao, H.; Jin, H.; Goodenough, J. B. Three Electron Reversible Redox Reaction in Sodium Vanadium Chromium Phosphate as a High-Energy-Density Cathode for Sodium-Ion Batteries. *Adv. Funct. Mater.* **2020**, *30*, No. 1908680.
(31) Zhu, T.; Hu, P.; Cai, C.; Liu, Z.; Hu, G.; Kuang, Q.; Mai, L.; Zhou, L. Dual Carbon Decorated $Na_3MnTi(PO_4)_3$: A high-Energy-Density Cathode Material for Sodium-Ion Batteries. *Nano Energy* **2020**, *70*, No. 104548.
(32) Zhou, W.; Xue, L.; Lu, X.; Gao, H.; Li, Y.; Xin, S.; Fu, G.; Cui, Z.; Zhu, Y.; Goodenough, J. B. $Na_xMV(PO_4)_3$ (M = Mn, Fe, Ni) Structure and Properties for Sodium Extraction. *Nano Lett.* **2016**, *16*, 7836−7841.
(33) Wang, D.; Wei, Z.; Lin, Y.; Chen, N.; Gao, Y.; Chen, G.; Song, L.; Du, F. Intercalation Pseudocapacitance in a NASICON-Structured $Na_2CrTi(PO_4)_3$@Carbon Nanocomposite: towards High-Rate and Long-Lifespan Sodium-Ion-Based Energy Storage. *J. Mater. Chem. A* **2019**, *7*, 20604−20613.
(34) Liu, X.; Jiang, X.; Zhong, F.; Feng, X.; Chen, W.; Ai, X.; Yang, H.; Cao, Y. High-Safety Symmetric Sodium-Ion Batteries Based on Nonflammable Phosphate Electrolyte and Double $Na_3V_2(PO_4)_3$ Electrodes. *ACS Appl. Mater. Interfaces* **2019**, *11*, 27833−27838.
(35) Dong, J.; Zhang, G.; Wang, X.; Zhang, S.; Deng, C. Cross-Linked $Na_2VTi(PO_4)_3$@C Hierarchical Nanofibers as High-Performance Bi-Functional Electrodes for Symmetric Aqueous Rechargeable Sodium Batteries. *J. Mater. Chem. A* **2017**, *5*, 18725−18736.
(36) Gao, H.; Goodenough, J. B. An Aqueous Symmetric Sodium-Ion Battery with NASICON-Structured $Na_3MnTi(PO_4)_3$. *Angew. Chem., Int. Ed.* **2016**, *55*, 12768−12772.
(37) Feng, Y.; Chen, S.; Wang, J.; Lu, B. Carbon Foam with Microporous Structure for High Performance Symmetric Potassium Dual-Ion Capacitor. *J. Energy Chem.* **2020**, *43*, 129−138.
(38) Wang, H.; Zhang, T.; Chen, C.; Ling, M.; Lin, Z.; Zhang, S.; Pan, F.; Liang, C. High-Performance Aqueous Symmetric Sodium-Ion Battery using NASICON-Structured $Na_2VTi(PO_4)_3$. *Nano Res.* **2018**, *11*, 490−498.
(39) Li, C.; Wu, W.; Wang, P.; Zhou, W.; Wang, J.; Chen, Y.; Fu, L.; Zhu, Y.; Wu, Y.; Huang, W. Fabricating an Aqueous Symmetric Supercapacitor with a Stable High Working Voltage of 2 V by Using an Alkaline-Acidic Electrolyte. *Adv. Sci.* **2019**, *6*, No. 1801665.
(40) Monkhorst, H. J.; Pack, J. D. Special Points for Brillouin-Zone Integrations. *Phys. Rev. B: Condens. Matter Mater. Phys.* **1976**, *13*, 5188−5192.
(41) Liechtenstein, A. I.; Anisimov, V. V.; Zaanen, J. Density-Functional Theory and Strong Interactions: Orbital Ordering in Mott-Hubbard Insulators. *Phys. Rev. B* **1995**, *52*, R5467−R5470.
(42) Jian, Z.; Sun, Y.; Ji, X. A New Low-Voltage Plateau of $Na_3V_2(PO_4)_3$ as an Anode for Na-ion Batteries. *Chem. Commun.* **2015**, *51*, 6381−6383.
(43) He, Q.; Yu, B.; Li, Z.; Zhao, Y. Density Functional Theory for Battery Materials. *Energy Environ. Mater.* **2019**, *2*, 264−279.
(44) Gao, H.; Li, Y.; Park, K.; Goodenough, J. B. Sodium Extraction from NASICON-Structured $Na_3MnTi(PO_4)_3$ through Mn(III)/Mn(II) and Mn(IV)/Mn(III) Redox Couples. *Chem. Mater.* **2016**, *28*, 6553−6559.
(45) Jian, Z.; Yuan, C.; Han, W.; Lu, X.; Gu, L.; Xi, X.; Hu, Y.-S.; Li, H.; Chen, W.; Chen, D.; Ikuhara, Y.; Chen, L. Atomic Structure and Kinetics of NASICON $Na_xV_2(PO_4)_3$ Cathode for Sodium-Ion Batteries. *Adv. Funct. Mater.* **2014**, *24*, 4265−4272.
(46) Zhu, T.; Hu, P.; Wang, X.; Liu, Z.; Luo, W.; Owusu, K. A.; Cao, W.; Shi, C.; Li, J.; Zhou, L.; Mai, L. Realizing Three-Electron Redox Reactions in NASICON-Structured $Na_3MnTi(PO_4)_3$ for Sodium-Ion Batteries. *Adv. Energy Mater.* **2019**, *9*, No. 1803436.
(47) Zhang, W.; Zhang, Z.; Li, H.; Wang, D.; Wang, T.; Sun, X.; Zheng, J.; Lai, Y. Engineering 3D Well-Interconnected $Na_4MnV(PO_4)_3$ Facilitates Ultrafast and Ultrastable Sodium Storage. *ACS Appl. Mater. Interfaces* **2019**, *11*, 35746−35754.
(48) Li, H.; Xu, M.; Gao, C.; Zhang, W.; Zhang, Z.; Lai, Y.; Jiao, L. Highly Efficient, Fast and Reversible Multi-Electron Reaction of $Na_3MnTi(PO_4)_3$ Cathode for Sodium-Ion Batteries. *Energy Storage Mater.* **2020**, *26*, 325−333.
(49) Xu, Y.; Wei, Q.; Xu, C.; Li, Q.; An, Q.; Zhang, P.; Sheng, J.; Zhou, L.; Mai, L. Layer-by-Layer $Na_3V_2(PO_4)_3$ Embedded in Reduced Graphene Oxide as Superior Rate and Ultralong-Life Sodium-Ion Battery Cathode. *Adv. Energy Mater.* **2016**, *6*, No. 1600389.
(50) He, S.; Wang, S.; Chen, H.; Hou, X.; Shao, Z. A New Dual-Ion Hybrid Energy Storage System with Energy Density Comparable to that of Ternary Lithium Ion Batteries. *J. Mater. Chem. A* **2020**, *8*, 2571−2580.

https://dx.doi.org/10.1021/acsami.0c05784
ACS Appl. Mater. Interfaces 2020, 12, 30328−30335